Applied Physics Letters

RESEARCH ARTICLE | AUGUST 16 2023

Aluminum scandium nitride films for piezoelectric transduction into silicon at gigahertz frequencies

L. Hackett ; M. Miller ; R. Beaucejour ; C. M. Nordquist ; J. C. Taylor ; S. Santillan ; R. H. Olsson ; M. Eichenfield

Appl. Phys. Lett. 123, 073502 (2023)
https://doi.org/10.1063/5.0151434

AIP Publishing

Applied Physics Letters ARTICLE pubs.aip.org/aip/apl

Aluminum scandium nitride films for piezoelectric transduction into silicon at gigahertz frequencies

Cite as: Appl. Phys. Lett. **123**, 073502 (2023); doi: 10.1063/5.0151434
Submitted: 21 March 2023 · Accepted: 21 July 2023 ·
Published Online: 16 August 2023

L. Hackett,[1] M. Miller,[1] R. Beaucejour,[2] C. M. Nordquist,[1] J. C. Taylor,[1] S. Santillan,[1] R. H. Olsson,[3] and M. Eichenfield[1,4,a)]

AFFILIATIONS

[1]Microsystems Engineering, Science, and Applications, Sandia National Laboratories, Albuquerque, New Mexico 87123, USA
[2]Department of Mechanical Engineering and Applied Mechanics, University of Pennsylvania, Philadelphia, Pennsylvania 19104, USA
[3]Department of Electrical and Systems Engineering, University of Pennsylvania, Philadelphia, Pennsylvania 19104, USA
[4]College of Optical Sciences, University of Arizona, Tucson, Arizona 85719, USA

[a)]Author to whom correspondence should be addressed: eichenfield@arizona.edu

ABSTRACT

Recent advances in the growth of aluminum scandium nitride films on silicon suggest that this material platform could be applied for quantum electromechanical applications. Here, we model, fabricate, and characterize microwave frequency silicon phononic delay lines with transducers formed in an adjacent aluminum scandium nitride layer to evaluate aluminum scandium nitride films, at 32% scandium, on silicon interdigital transducers for piezoelectric transduction into suspended silicon membranes. We achieve an electromechanical coupling coefficient of 2.7% for the extensional symmetric-like Lamb mode supported in the suspended material stack and show how this coupling coefficient could be increased to at least 8.5%, which would further boost transduction efficiency and reduce the device footprint. The one-sided transduction efficiency, which quantifies the efficiency at which the source of microwave photons is converted to microwave phonons in the silicon membrane, is 10% at 5 GHz at room temperature and, as we discuss, there is a path to increase this toward near-unity efficiency based on a combination of modified device design and operation at cryogenic temperatures.

Electromechanical components are becoming increasingly important for the transduction and storage of quantum information.[1,2] The coupling of phononic devices to superconducting qubits through piezoelectric transduction[3] could lead to quantum memories in silicon (Si) phononic resonators with ultra-long lifetimes limited by two-level system defects at cryogenic temperatures.[4,5] Piezoelectric transduction has also been applied to demonstrate remote-entanglement between two superconducting qubits mediated by an itinerant phonon[6] and to quantum transduction schemes for quantum networking, where a microwave phonon serves as an intermediary between a microwave and optical photon.[2,7,8] An ongoing challenge in the field is to produce electromechanical devices that can be integrated with state-of-the-art nanobeam Si phononic resonators[4] and optomechanical crystals[9] while achieving efficient and broadband phonon injection into the Si. Aluminum nitride (AlN) is a back-end-of-line CMOS-compatible piezoelectric material that can be grown directly on Si and selectively removed,[10,11] enabling piezoelectric transduction to occur in isolated areas on a chip[8] and the remaining routing, processing, and storage of acoustic signals to occur in the Si. Yet, the maximum achievable electromechanical coupling coefficient (k^2) for AlN is generally small and this limits the piezoelectric transduction efficiency of devices. The k^2 value characterizes the ratio between the converted mechanical power and the supplied electrical power. Lithium niobate[12] and lithium tantalate[13] can achieve k^2 values exceeding AlN, but producing thin films of these materials on Si is challenging.[14]

By incorporating scandium (Sc) to produce aluminum scandium nitride ($Al_{1-x}Sc_xN$) alloy films, the combination of changing material parameters leads to a larger k^2 than AlN.[15,16] However, until recently, $Al_{1-x}Sc_xN$ films could not be grown directly on Si with low anomalous grain density and in a stress neutral state.[17] This is critical as anomalous grains increase loss through scattering and prevent selective etching of the films.[17] In addition, stress can cause delamination of films on a substrate and bending or buckling for suspended structures. While quantum systems that utilize piezoelectric transduction have been rapidly emerging,[14] the limits to piezoelectric transduction efficiency, and therefore, overall system losses, remain greatly unexplored.

Here, we study the fundamental loss mechanisms and limitations for a new material system of $Al_{1-x}Sc_xN$ patterned on Si.

In an electromechanical transducer design, the transduction efficiency can be increased by increasing the number of electrodes, N, and increasing k^2.[18,19] However, increasing N decreases the operating bandwidth, and large N can also lead to deleterious effects, such as increased transducer propagation losses, deep Bragg reflection resonances, excess resistive losses in the metal, and the creation of coupled cavities.[18,19] A larger k^2 can enable a smaller device footprint, a larger operating bandwidth, and simpler impedance matching to sources.[18,19] A significant source of loss in this work occurs from an acoustic reflection at the $Al_{0.68}Sc_{0.32}N$–Si/Si interface. With a larger k^2, there is more flexibility to reduce the $Al_{0.68}Sc_{0.32}N$ film thickness, which will reduce this loss.

Here, we evaluate piezoelectric transduction efficiency into a Si membrane at room temperature using an $Al_{0.68}Sc_{0.32}N$–Si interdigital transducer (IDT). We demonstrate a one-sided transduction efficiency, which quantifies the efficiency at which the source of microwave photons is converted to microwave phonons in the Si, of 10% at 5 GHz; we then discuss how to increase this toward near-unity efficiency. We achieve a k^2 of 2.7% at 5 GHz for the symmetric-like ($\tilde{S}_0$) Lamb mode supported in a material stack of 250 nm thick $Al_{0.68}Sc_{0.32}N$ grown on a 250 nm thick Si membrane with intermediate AlN seed (15 nm thick) and gradient (35 nm thick) layers, which have been shown to reduce abnormally oriented grains (AOGs).[17] The tilde labeling the modes ($\tilde{A}_0$, $\tilde{A}_1$, $\tilde{S}_0$, etc.) indicates that the Lamb modes in the $Al_{0.68}Sc_{0.32}N$–Si stack lack vertical symmetry and instead are similar to the symmetric or antisymmetric Lamb modes. The Lamb modes in the Si membrane do satisfy the vertical symmetry requirements and, therefore, the desired symmetric (S_0) output mode is supported. Through modeling, we also show how k^2 could be increased to exceed 8.5% in the future work, which would increase the transduction efficiency by allowing more design flexibility in the electrodes and material stack that strongly influence loss.

Figure 1(a) shows a scanning electron microscope (SEM) image of the device structure utilized to evaluate the piezoelectric transduction efficiency. The device consists of input and output IDTs, which are both on a suspended membrane of $Al_{1-x}Sc_xN$ on Si. In-between the IDTs, the $Al_{1-x}Sc_xN$ is selectively removed such that only a suspended Si waveguide approximately the same width as the transducer remains. Figure 1(b) shows the modeled displacement, from a 2D finite element method (FEM) study, for the antisymmetric-like ($\tilde{A}_0$ and $\tilde{A}_1$) and symmetric-like ($\tilde{S}_0$) Lamb modes in a stack of a 300 nm thick piezoelectric film on 250 nm Si. The material parameters that we utilize for AlN and $Al_{0.68}Sc_{0.32}N$ are given in Table I.[15,16,20] We target the S_0 mode in Si because it is the mode that would most strongly optomechanically couple to photons in the membrane and is most closely related to the modes that have been used to demonstrate >1 s lifetimes in suspended Si phononic crystals.[4] The transducer $\tilde{S}_0$ mode is targeted as we expect it to efficiently excite the S_0 mode in the Si and it has the highest k^2 of the available modes.

The one-sided transduction path is illustrated in Fig. 1(c). The source generates microwave photons, which are then converted to $\tilde{S}_0$ microwave phonons in the $Al_{0.68}Sc_{0.32}N$–Si stack by the IDT. These $\tilde{S}_0$ microwave phonons are then transmitted into the Si membrane as S_0 phonons. Here we utilize a two-port device [Fig. 1(a)] as highly accurate measurements can be made of the total end-to-end radio

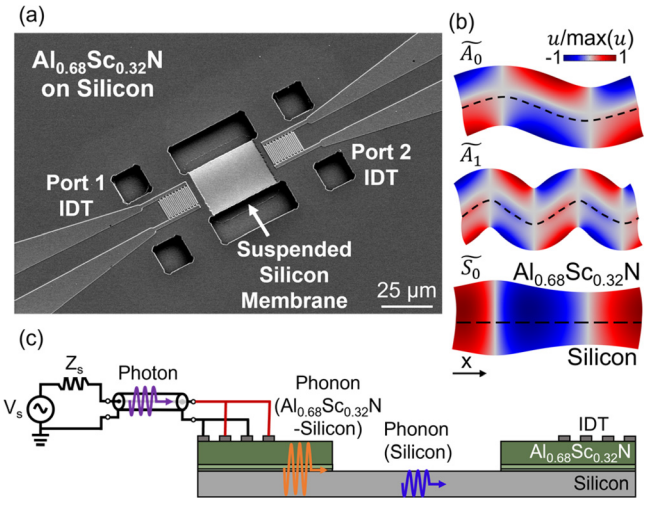

FIG. 1. (a) SEM image of the suspended $Al_{0.68}Sc_{0.32}N$–Si IDTs and the Si membrane. (b) 2D FEM models of the x-displacement (u) for the antisymmetric-like ($\tilde{A}_0$ and $\tilde{A}_1$) and symmetric-like ($\tilde{S}_0$) Lamb modes in the $Al_{0.68}Sc_{0.32}N$–Si stack. (c) Schematic illustrating the one-sided transduction path from microwave photon (purple) to microwave phonon in the Si (blue) with an intermediary microwave phonon in the $Al_{0.68}Sc_{0.32}N$–Si (orange).

frequency losses using a network analyzer. We then assume that the device is symmetric along the propagation direction, as supported by scattering parameter (S-parameter) measurements, to obtain the one-sided transduction efficiency.

To understand the improvements provided by the Sc, we modeled the expected k^2 values for $Al_{0.68}Sc_{0.32}N$ and AlN for the $\tilde{S}_0$ mode as a function of piezoelectric film thickness [Fig. 2(a)]. Here, k^2 is calculated using the standard definition of $k^2 = 2\left|\frac{\Delta v}{v}\right|$, where v is the acoustic velocity with an electrically open boundary condition on the surface of the piezoelectric film and Δv is the difference between the acoustic velocity for electrically open and electrically shorted boundary conditions. In this work, the total piezoelectric film thickness is 300 nm, corresponding to a modeled k^2 value of 2.9%.

TABLE I. Material parameters for modeling of the AlN and $Al_{0.68}Sc_{0.32}N$ piezoelectric films.

		AlN	$Al_{0.68}Sc_{0.32}N$
Density	ρ	3.23 g/cm^3	3.32 g/cm^3
Elastic matrix	c_{11}	410 GPa	307 GPa
	c_{12}	149 GPa	147 GPa
	c_{13}	99 GPa	123 GPa
	c_{33}	389 GPa	230 GPa
	c_{44}	124 GPa	110 GPa
	c_{66}	c_{11}-c_{12}/2	c_{11}-c_{12}/2
Piezoelectric matrix	e_{15}	−0.48 C/m^2	−0.23 C/m^2
	e_{31}	−0.58 C/m^2	−0.69 C/m^2
	e_{33}	1.55 C/m^2	2.80 C/m^2
Relative permittivity	ε_r	9	15

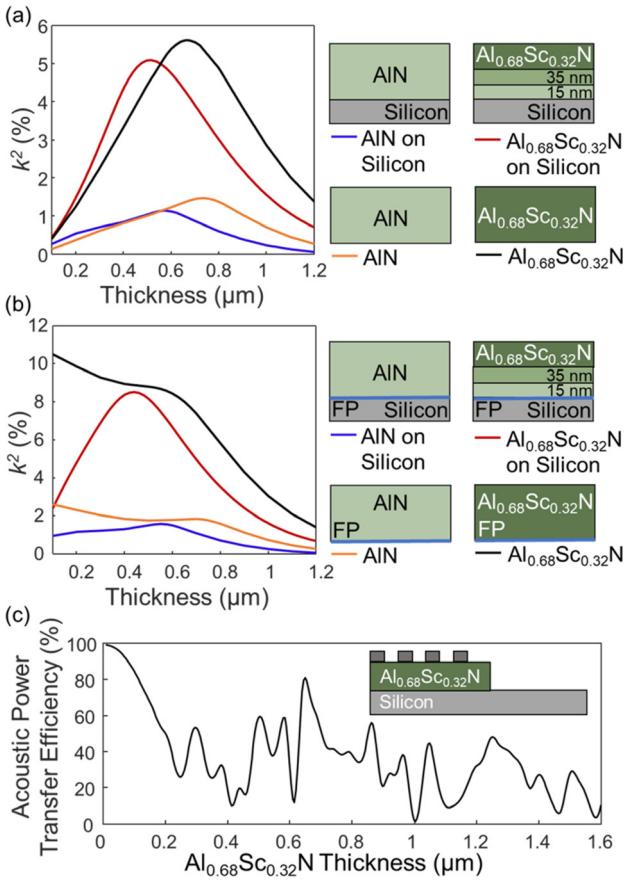

FIG. 2. Modeled k^2 values as a function of piezoelectric thickness for (a) top-only and (b) floating potential bottom electrode configurations. (c) Modeled acoustic power transfer efficiency as a function of the $Al_{0.68}Sc_{0.32}N$ thickness.

Figure 2(b) shows the modeled k^2 values as a function of the piezoelectric film thicknesses with a floating potential boundary condition placed at the bottom boundary of the piezoelectric layers. The modeled k^2 value can be increased up to 8.5% as the bottom electrode better concentrates the electric field in the $Al_{0.68}Sc_{0.32}N$. This type of electrode configuration could be achieved in the future work by patterned doping of the Si before the $Al_{1-x}Sc_xN$ growth. For high enough doping levels ($>3 \times 10^{18}$ cm^{-3}) semi-metallic behavior is achieved in the Si.[21] Losses occur at cryogenic temperatures in degenerately doped Si,[22,23] yet the expected limited quality factor corresponds to only ~0.0008 dB of propagation loss in the transducer assuming propagation entirely in the Si.[22] While high doping of a Si phononic resonator may increase the losses beyond what can be tolerated for quantum phononic applications, patterned doping of the Si device layer in isolated transducer regions can be accomplished through the use of an implant mask. With this approach, high efficiency piezoelectric transduction into Si could be achieved in the isolated regions while the remaining Si on the chip retains its original purity.

Figure 2(c) shows a plot of the modeled acoustic power transfer efficiency, η, at the $Al_{0.68}Sc_{0.32}N$–Si/Si interface as a function of $Al_{0.68}Sc_{0.32}N$ thickness. The reduction in η from unity is due to the reflection that occurs from the acoustic impedance mismatch at the interface where the $Al_{1-x}Sc_xN$ is selectively removed to produce the S_0 mode in the Si. To evaluate η, the output power is computed from a 2D FEM model of the IDT and phononic waveguide for the cases where the $Al_{0.68}Sc_{0.32}N$ remains after the IDT (P_{OUT}) and where it is removed leaving only the Si waveguide ($P_{OUT,Si}$). The efficiency is given by $\eta = P_{OUT,Si}/P_{OUT}$, where $P_{OUT,Si} = \int \mathrm{Re}[P_a]dl$, $P_{OUT} = \int \mathrm{Re}[P_{\mathrm{piezo}}]dl$, P_a is the complex acoustic Poynting vector, and P_{piezo} is the complex piezoelectric Poynting vector.[24] To minimize this loss mechanism, the piezoelectric film should be as thin as possible. At a film thickness of 300 nm, the acoustic power transfer efficiency is 51%, while for a film thickness of 100 nm, the acoustic power transfer efficiency increases to 90%. However, k^2 is optimized at a thickness significantly larger than 100 nm.

The developed fabrication process flow for this work is shown in Fig. 3. A 300 nm piezoelectric film is grown on a Si on insulator (SOI) wafer with a 250 nm Si device layer thickness and a 3 μm buried oxide (BOX) thickness. The $Al_{1-x}Sc_xN$ was deposited at 350 °C via pulsed DC reactive co-sputtering from separate 4 in. aluminum (1 kW) and Sc (555 W) targets in an Evatec CLUSTERLINE® 200 II physical vapor deposition system under process conditions previously reported by Beaucejour *et al.*[17] To achieve a slightly tensile stress at a 300 nm thickness, a gas flow of 30 sccm pure nitrogen (N_2) was utilized during sputter deposition. A slightly tensile stress ensures flat device membranes. To ensure a low number of AOGs when depositing $Al_{1-x}Sc_xN$ on Si, a seed layer consisting of 15 nm of AlN and a gradient layer consisting of 35 nm where the Sc cathode power is linearly varied from 0 to 555 W through the thickness is utilized.[25] This is followed by deposition of a 250 nm thick $Al_{0.68}Sc_{0.32}N$ layer resulting in a total piezoelectric layer thickness of 300 nm. For the 300 nm thick piezoelectric film, the measured rocking curve full-width half maximum is 2.36°.

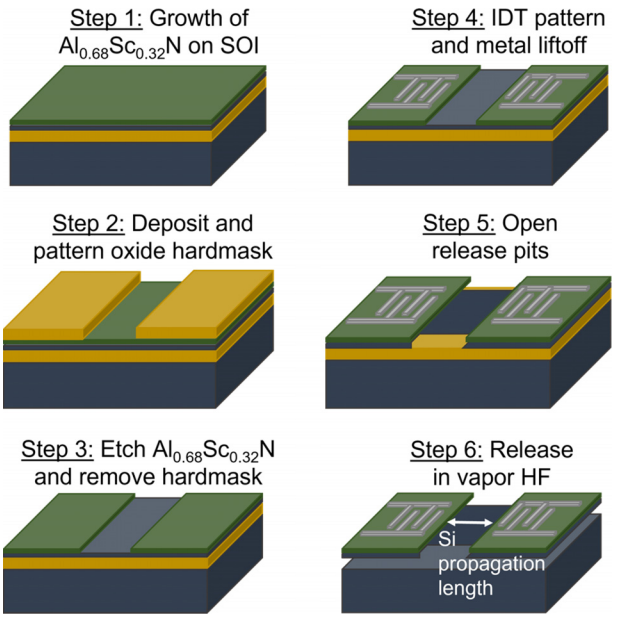

FIG. 3. $Al_{0.68}Sc_{0.32}N$–Si electromechanical devices process flow.

The 250 nm $Al_{0.68}Sc_{0.32}N$ film is etched, with the use of an oxide hard mask, by inductively coupled plasma reactive ion etching (ICP-RIE) utilizing chlorine and boron trichloride gas chemistry. As any exposed Si could be significantly damaged by the ICP-RIE process, a heated solution of 1:1:10 sulfuric acid, hydrogen peroxide, and water is used to clear the seed and gradient layers without attacking the Si device layer once the $Al_{0.68}Sc_{0.32}N$ layer is etched. The IDTs are patterned via e-beam lithography followed by a metal liftoff of a 100 nm aluminum layer with a 10 nm chrome adhesion layer. An etch in the field lands in the BOX to form the release pits. The devices are then suspended by selective etching of the BOX in a vapor of anhydrous hydrofluoric acid.

We evaluated the transduction efficiency by measuring the S-parameters on a calibrated network analyzer. The measured S-parameters as a function of frequency for a device with a 100 μm Si propagation length are shown in Fig. 4(a). The IDTs have a split finger configuration designed for an acoustic wavelength of 1.6 μm, apertures of 15 μm, and lengths of 50 acoustic wavelengths, which corresponds to 200 $\Lambda/8$ electrodes for each IDT. The split finger configuration suppresses the Bragg grating resonant reflection that occurs for an IDT with electrode widths of $\Lambda/4$.[26]

There are four prominent transmission peaks in Fig. 4(a) with the corresponding modeled displacement fields shown in Fig. 4(b). The $\tilde{S}_0$ mode is generated in the $Al_{0.68}Sc_{0.32}N$–Si suspended IDT at a resonance frequency of 5 GHz. The S_{11} and S_{21} values as a function of frequency for this mode are shown in Fig. 4(c). The total end-to-end losses for the two-port device are 19.6 dB at 5 GHz, which corresponds to a one-sided loss of 9.8 dB and, therefore, a one-sided transduction efficiency of 10%. The electromechanical admittance, $Y = G + iB$, where G is the radiation conductance and B is the radiation susceptance, for this mode is plotted in Fig. 4(d). We fit the experimental data to a Mason equivalent circuit model[19] [Fig. 4(e)] to extract k^2. The expression for G is given by $G(f) = 8k^2 f_0 C_T N \frac{\sin^2 X}{X^2}$, where f_0 is the IDT resonance frequency, $C_T = AC_s$ is the transducer capacitance, N is the number of electrodes, A is the transducer area, C_s is the capacitance per unit area, and $X = N\pi\frac{f-f_0}{f_0}$. As described previously,[27] k^2 can be found according to $k^2 = \frac{\pi}{4}\frac{1}{\omega_0^2 C_s A}\int G(\omega)d\omega$, where $\omega_0 = 2\pi f_0$ is the angular resonance frequency. The fitting does not differentiate between mechanical radiation and other dissipation mechanisms, such as ohmic losses, and the resulting k^2 value is significantly larger than the true value if the non-mechanical dissipation is not removed. Thus, the resistive losses have been removed from the data shown in Fig. 4(c) and used to compute the data in Fig. 4(d), which was then numerically integrated to determine k^2. Figure 4(e) shows a plot of the k^2 values for 100, 200, and 300 nm piezoelectric films on a 250 nm Si membrane with a comparison to the modeled values. For the 300 nm piezoelectric film on a 250 nm thick Si membrane, a k^2 of 2.7% is achieved experimentally at 5 GHz. For a 200 nm film on Si, a k^2 of 0.9% is found and for a 100 nm film on Si, the value is 0.3%.

Table II summarizes the one-sided losses and the potential mitigation methods. To determine the impedance mismatch loss, the S-parameter data were imported into Keysight Advanced Design System (ADS) and a matching network to a 50 Ω source was implemented. By this method, we found the impedance mismatch loss to be 0.5 dB for a single IDT. A significant source of loss is due to resistive losses. For an electromechanical transducer, the S_{11} value is ideally a very large

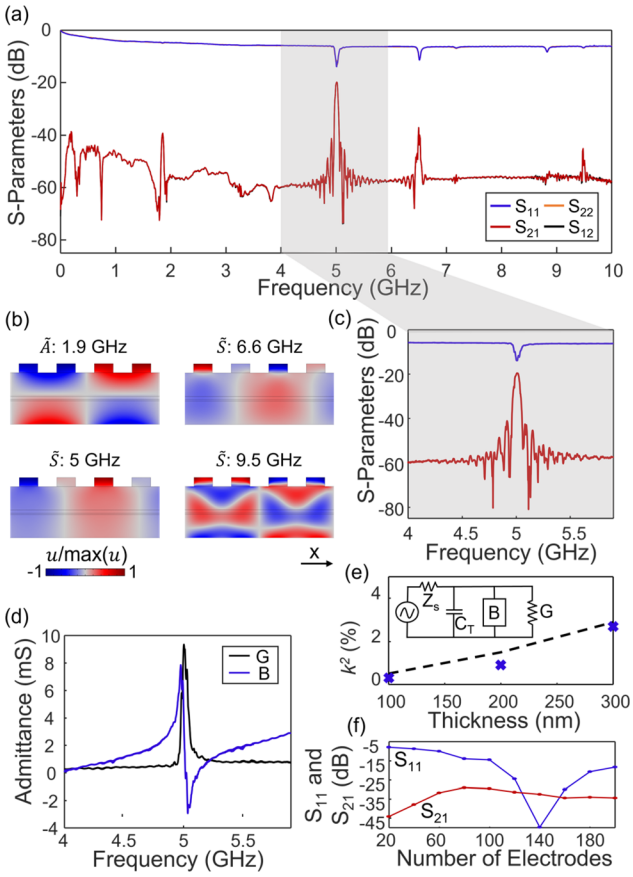

FIG. 4. (a) S-parameters as a function of frequency for a device with $\Lambda = 1.6$ μm and a Si propagation length of 100 μm. (b) Modeled x-displacement, u, for the Lamb modes corresponding to the four prominent transmission peaks with either antisymmetric-like ($\tilde{A}$) or symmetric-like ($\tilde{S}$) polarization. (c) Plots of the measured S_{11} and S_{21} as a function of frequency for the $\tilde{S}_0$ mode along with the (d) electromechanical admittance. (e) Measured (blue markers) and modeled (dashed black line) k^2 values as a function of the $Sc_{0.32}Al_{0.68}N$ thickness. The Mason equivalent circuit model is shown in the inset. (f) Minimum S_{11} and maximum S_{21} as a function of number of electrodes for a $Sc_{0.32}Al_{0.68}N$–Si acoustic delay line with no exposed Si and an aperture of 10 μm.

TABLE II. Loss mechanisms and mitigation for the one-sided transduction path.

Mechanism	Value (dB)	Mitigation
Impedance mismatch	0.5	Increase k^2, cryogenic operation, microwave cavity coupling
Resistive losses	2.9–3.2	Increase k^2, cryogenic operation
Bi-directional IDT	3	Back reflector, unidirectional IDT
Reflection at $Al_{0.68}Sc_{0.32}N$–Si/Si	1–3	Increase k^2, thinner film, acoustic grating
Acoustic propagation loss	0.1–2.4	Cryogenic operation

negative value in the passband, which indicates that the power is efficiently radiated as phonons with little reflection. However, outside of the transducer passband this radiation does not occur and deviations of S_{11} from 0 dB are due to resistive losses in the materials. We find this loss to be 2.9–3.2 dB per IDT, which we primarily attribute to ohmic losses in the metal. In addition, a loss of 3 dB is due to the bidirectional IDT design, which can be eliminated in future work by using a back reflector or a unidirectional IDT.

If the intended application space is quantum transduction, then in order to operate the system free of thermal occupation of phononic states, the system would operate at a temperature less than ~50 mK for 5 GHz, where the aluminum metal would be superconducting below its transition temperature of 1.2 K.[28] We anticipate that this would eliminate resistive losses in the IDT in the case, where the chrome adhesion layer is removed and the aluminum is directly deposited onto the $Al_{0.68}Sc_{0.32}N$ following a sputter etch to remove the native oxide layer.[29] In addition, the source impedance may be significantly larger than 50 Ω, such as if the actual source of phonons is a microwave cavity or microwave qubit, which would enable impedance matching with a smaller number of electrodes. The loss from the reflection at the $Al_{0.68}Sc_{0.32}N$–Si/Si interface can be estimated from modeling results [Fig. 2(c)]. We modeled a variety of sidewall angles and found that the reflection loss has a range of 1–3 dB per interface. The remaining 0.1–2.4 dB of loss is assumed to be from propagation losses. Some sources of propagation loss, such as those that are thermal in nature, are eliminated at cryogenic temperatures.[4,11]

Reduced IDT apertures could provide transduction into Si membranes with reduced widths, yet they require a larger N, which then exacerbates propagation losses in the transducer and resistive losses. To confirm this trade-off, we measured the S-parameters as a function of frequency for a series of devices with an IDT aperture of 10 μm, no exposed Si membrane, a propagation length of 100 μm, electrodes widths of $\Lambda/4$, and varying N. Figure 4(f) shows the minimum S_{11} and maximum S_{21} as a function of N. The minimum S_{11}, which corresponds to the best impedance matching to the 50 Ω source, occurs when $N = 140$, while the maximum S_{21} value, which corresponds to the minimum total insertion loss, occurs at a significantly smaller number of electrodes ($N = 80$). Further increasing k^2 would enable more efficient transduction into Si membranes with smaller widths, especially when combined with acoustic horns[27] or focusing transducers.[30]

Here, we have demonstrated a one-sided transduction efficiency of 10% at 5 GHz in an $Al_{0.68}Sc_{0.32}N$ on Si material platform and discussed a path toward achieving near-unity efficiency based on modified device design and operation at cryogenic temperatures. We have demonstrated a k^2 of 2.7% at 5 GHz, showed how k^2 could be increased to exceed 8.5%, and discussed how improvements in k^2 affect transduction efficiency. The 32% Sc concentration could also be increased, up to 42%, with further optimization of growth conditions, which would significantly increase the piezoelectric coefficients beyond what has been utilized here.[15] Approaches that require further development include focusing IDTs[30] or horns[27] to couple into wavelength-scale Si phononic waveguides. Acoustic gratings could also eliminate the acoustic reflection loss at the $Al_{0.68}Sc_{0.32}N$–Si/Si interface. With the ability to grow these films with low anomalous grains in a stress neutral state, $Al_{0.68}Sc_{0.32}N$ on Si is a promising addition to the material platforms available for quantum transduction and quantum information processing utilizing electromechanical components.

This work was funded in part by the NSF CAREER Award (1944248). This work was carried out in part at the Singh Center for Nanotechnology at the University of Pennsylvania, a member of the National Nanotechnology Coordinated Infrastructure (NNCI) network, which is supported by the National Science Foundation (Grant No. HR0011-21-9-0004). This work was supported, in part, by the U.S. Department of Energy, Office of Science, Advanced Scientific Computing Research (ASCR) under FWP 19-022266 "Quantum Transduction and Buffering Between Microwave Quantum Information Systems and Flying Optical Photons in Fibers." The authors performed this work, in part, at the Center for Integrated Nanotechnologies, an Office of Science User Facility operated for the U.S. Department of Energy (DOE) Office of Science. Additional supported was provided by the Laboratory Directed Research and Development program at Sandia National Laboratories, a multimission laboratory managed and operated by National Technology and Engineering Solutions of Sandia, LLC., a wholly owned subsidiary of Honeywell International, Inc., for the U.S. Department of Energy's National Nuclear Security Administration under Contract No. DE-NA-003525. This paper describes objective technical results and analysis. Any subjective views or opinions that might be expressed in the paper do not necessarily represent the views of the U.S. Department of Energy or the United States Government.

AUTHOR DECLARATIONS

Conflict of Interest

The authors have no conflicts to disclose.

Author Contributions

Lisa Hackett: Conceptualization (supporting); Investigation (lead); Methodology (lead); Writing – original draft (lead); Writing – review & editing (equal). **Michael Miller:** Investigation (supporting). **Rossiny Beaucejour:** Investigation (supporting). **Courtney Nordquist:** Investigation (supporting); Methodology (supporting). **Jeff Taylor:** Investigation (supporting). **Steven Santillan:** Investigation (supporting); Methodology (supporting). **Roy Harold Olsson III:** Conceptualization (supporting); Supervision (supporting). **Matt Eichenfield:** Conceptualization (lead); Formal analysis (equal); Methodology (equal); Project administration (equal); Resources (equal); Supervision (lead); Writing – review & editing (equal).

DATA AVAILABILITY

The data that support the findings of this study are available from the corresponding author upon reasonable request.

REFERENCES

[1]K. C. Balram and K. Srinivasan, Adv. Quantum Technol. **5**(3), 2100095 (2022); A. Bienfait, K. J. Satzinger, Y. P. Zhong, H.-S. Chang, M.-H. Chou, C. R. Conner, É. Dumur, J. Grebel, G. A. Peairs, and R. G. Povey, Science **364**(6438), 368 (2019); X. Han, W. Fu, C.-L. Zou, L. Jiang, and H. X. Tang, Optica **8**(8), 1050 (2021); N. J. Lambert, A. Rueda, F. Sedlmeir, and H. G. L. Schwefel, Adv. Quantum Technol. **3**(1), 1900077 (2020); R. Manenti, A. F. Kockum, A. Patterson, T. Behrle, J. Rahamim, G. Tancredi, F. Nori, and P. J. Leek, Nat. Commun. **8**(1), 975 (2017); L. Tian, Ann. Phys. **527**(1–2), 1 (2015); T. P. McKenna, J. D. Witmer, R. N. Patel, W. Jiang, R. Van Laer, P. Arrangoiz-

Arriola, E. Alex Wollack, J. F. Herrmann, and A. H. Safavi-Naeini, Optica **7**(12), 1737 (2020); H. Ramp, T. J. Clark, B. D. Hauer, C. Doolin, K. C. Balram, K. Srinivasan, and J. P. Davis, Appl. Phys. Lett. **116**(17), 174005 (2020); A. P. Higginbotham, P. S. Burns, M. D. Urmey, R. W. Peterson, N. S. Kampel, B. M. Brubaker, G. Smith, K. W. Lehnert, and C. A. Regal, Nat. Phys. **14**(10), 1038 (2018).

[2]M. Forsch, R. Stockill, A. Wallucks, I. Marinković, C. Gärtner, R. A. Norte, F. van Otten, A. Fiore, K. Srinivasan, and S. Gröblacher, Nat. Phys. **16**(1), 69 (2020).

[3]P. Arrangoiz-Arriola and A. H. Safavi-Naeini, Phys. Rev. A **94**(6), 063864 (2016); Y. Chu, P. Kharel, W. H. Renninger, L. D. Burkhart, L. Frunzio, P. T. Rakich, and R. J. Schoelkopf, Science **358**(6360), 199 (2017); M. Pechal, P. Arrangoiz-Arriola, and A. H. Safavi-Naeini, Quantum Sci. Technol. **4**(1), 015006 (2018).

[4]G. S. MacCabe, H. Ren, J. Luo, J. D. Cohen, H. Zhou, A. Sipahigil, M. Mirhosseini, and O. Painter, Science **370**(6518), 840 (2020).

[5]R. O. Behunin, F. Intravaia, and P. T. Rakich, Phys. Rev. B **93**(22), 224110 (2016); B. D. Hauer, P. H. Kim, C. Doolin, F. Souris, and J. P. Davis, *ibid.* **98**(21), 214303 (2018).

[6]É. Dumur, K. J. Satzinger, G. A. Peairs, M.-H. Chou, A. Bienfait, H.-S. Chang, C. R. Conner, J. Grebel, R. G. Povey, and Y. P. Zhong, npj Quantum Inf. **7**(1), 173 (2021).

[7]W. Jiang, C. J. Sarabalis, Y. D. Dahmani, R. N. Patel, F. M. Mayor, T. P. McKenna, R. Van Laer, and A. H. Safavi-Naeini, Nat. Commun. **11**(1), 1166 (2020); A. Khurana, P. Jiang, and K. C. Balram, Phys. Rev. Appl. **18**(5), 054030 (2022); I. Marinković, M. Drimmer, B. Hensen, and S. Gröblacher, Nano Lett. **21**(1), 529 (2021).

[8]M. Mirhosseini, A. Sipahigil, M. Kalaee, and O. Painter, Nature **588**(7839), 599 (2020).

[9]J. Chan, T. P. Mayer Alegre, A. H.Safavi-Naeini, J. T. Hill, A. Krause, S. Gröblacher, M. Aspelmeyer, and O. Painter, Nature **478**(7367), 89 (2011); J. Chan, A. H. Safavi-Naeini, J. T. Hill, S. Meenehan, and O. Painter, Appl. Phys. Lett. **101**(8), 081115 (2012).

[10]L. Fan, X. Sun, C. Xiong, C. Schuck, and H. X. Tang, Appl. Phys. Lett. **102**(15), 153507 (2013); K. E. Wojciechowski, M. S. Baker, P. J. Clews, and R. H. Olsson, J. Microelectromech. Syst. **24**(6), 1782 (2015).

[11]P. R. Stanfield, A. J. Leenheer, C. P. Michael, R. Sims, and M. Eichenfield, Opt. Express **27**(20), 28588 (2019).

[12]R. Lu, Y. Yang, M.-H. Li, T. Manzaneque, and S. Gong, IEEE Trans. Ultrason. Ferroelectr. Freq. Control **67**(2), 402 (2020).

[13]I. E. Kuznetsova, B. D. Zaitsev, S. G. Joshi, and I. A. Borodina, IEEE Trans. Ultrason. Ferroelectr. Freq. Control **48**(1), 322 (2001).

[14]P. Arrangoiz-Arriola, *Quantum Acoustics with Lithium Niobate Nanostructures* (Stanford University, 2019); J. Wu, S. Zhang, L. Zhang, H. Zhou, P. Zheng, H. Yao, Z. Li, K. Huang, T. Wu, and X. Ou, IEEE Trans. Ultrason. Ferroelectr. Freq. Control **69**(8), 2579 (2022).

[15]M. Akiyama, K. Umeda, A. Honda, and T. Nagase, Appl. Phys. Lett. **102**(2), 021915 (2013).

[16]N. Kurz, A. Ding, D. F. Urban, Y. Lu, L. Kirste, N. M. Feil, A. Žukauskaitė, and O. Ambacher, J. Appl. Phys. **126**(7), 075106 (2019).

[17]R. Beaucejour, V. Roebisch, A. Kochhar, C. G. Moe, M. D. Hodge, and R. H. Olsson, J. Microelectromech. Syst. (published online 2022).

[18]S. Datta, *Surface Acoustic Wave Devices*. (Prentice Hall, 1986).

[19]C. S. Hartmann, D. T. Bell, R. C. Rosenfeld, E. Royer, and D. Dieulesaint, IEEE Trans. Microwave Theory Techn. **21**(4), 162 (1973); D. Royer and E. Dieulesaint, *Elastic Waves in Solids II: Generation, Acousto-Optic Interaction, Applications* (Springer Science & Business Media, 1999).

[20]M. A. Caro, S. Zhang, T. Riekkinen, M. Ylilammi, M. A. Moram, O. Lopez-Acevedo, J. Molarius, and T. Laurila, J. Phys.: Condens. Matter **27**(24), 245901 (2015).

[21]N. Mikoshiba, Rev. Mod. Phys. **40**(4), 833 (1968); N. F. Mott, Philos. Mag. **6**(62), 287 (1961).

[22]E. Hwang and S. A. Bhave, in *IEEE 24th International Conference on Micro Electro Mechanical Systems* (IEEE, 2011).

[23]W. P. Mason and T. B. Bateman, Phys. Rev. Lett. **10**(5), 151 (1963).

[24]B. A. Auld, *Acoustic Fields and Waves in Solids* (Рипол Классик, 1973).

[25]R. Beaucejour, M. D'Agati, K. Kalyan, and R. H. Olsson III, Micromachines **13**(8), 1169 (2022).

[26]L. R. Sletten, University of Colorado at Boulder, 2021.

[27]Y. D. Dahmani, C. J. Sarabalis, W. Jiang, F. M. Mayor, and A. H. Safavi-Naeini, Phys. Rev. Appl. **13**(2), 024069 (2020).

[28]J. F. Cochran and D. E. Mapother, Phys. Rev. **111**(1), 132 (1958).

[29]G. Esteves, T. R. Young, Z. Tang, S. Yen, T. M. Bauer, M. D. Henry, and R. H. Olsson III, Appl. Phys. Lett. **118**(17), 171902 (2021).

[30]M. Eichenfield and R. H. Olsson, in *IEEE International Ultrasonics Symposium (IUS)* (IEEE, 2013).